Geophysical Research Letters

RESEARCH LETTER
10.1029/2019GL082746

Joint Inversion of Rayleigh Wave Phase Velocity, Particle Motion, and Teleseismic Body Wave Data for Sedimentary Structures

Guoliang Li[1,2], **Fenglin Niu**[1,3], **Yingjie Yang**[2], **and Kai Tao**[1]

[1]State Key Laboratory of Petroleum Resource and Prospecting, and Unconventional Petroleum Research Institute, China University of Petroleum at Beijing, Beijing, China, [2]Australian Research Council Centre of Excellence for Core to Crust Fluid Systems and GEMOC, and Department Of Earth and Planetary Science, Macquarie University, North Ryde, New South Wales, Australia, [3]Department of Earth, Environmental and Planetary Sciences, Rice University, Houston, TX, USA

Key Points:
- Rayleigh wave phase velocity, particle motion, and teleseismic body wave data are jointly inverted for high-resolution sedimentary models
- The high-resolution sedimentary models are used to effectively extract deep structural signals by removing sediment reverberations
- The method can be extended to single-station recordings by excluding the Rayleigh wave phase velocity

Supporting Information:
- Supporting Information S1
- Data Set S1

Correspondence to:
F. Niu,
niu@rice.edu

Citation:
Li, G., Niu, F., Yang, Y., & Tao, K. (2019). Joint inversion of Rayleigh wave phase velocity, particle motion, and teleseismic body wave data for sedimentary structures. *Geophysical Research Letters*, *46*. https://doi.org/10.1029/2019GL082746

Received 11 MAR 2019
Accepted 28 MAY 2019
Accepted article online 5 JUN 2019

Abstract Mapping seismic structures of sedimentary basins is of great importance to better evaluate energy resources and seismic hazards. In this study, we develop a joint Bayesian Monte Carlo nonlinear inversion method that utilizes the complementary nature of Rayleigh wave phase velocity, Rayleigh wave particle motion, and teleseismic *P* wave in responding to sedimentary structures. Synthetic tests demonstrate that our joint inversion can retrieve the input sedimentary models better than inversions with surface or body wave data alone. We apply our method to waveform data of two broadband stations inside the Songliao Basin in northeast China to invert for sedimentary structures beneath the two stations. We verify our results by successfully isolating the Moho *P*-to-*S* conversion from sediment reverberations in surface receiver functions with a wavefield-downward-continuation technique. We further demonstrate that we can extend our method to single-station inversions by excluding the Rayleigh wave phase velocity in the inversion.

1. Introduction

Sedimentary basins contain rich natural resources, such as petroleum, natural gas, and coal, providing vital resources for the development of human societies. Knowing detailed structures of sedimentary layers is essential to better explore these resources. On the other hand, seismic waves can be significantly amplified once they propagate into a sediment layer due to its low velocity and density, making sedimentary basins more vulnerable to seismic hazards (e.g., Bonilla et al., 1997; Hough et al., 1990). A good example is the 1985 Mexico earthquake (Mw=8.0), which caused severe damage to Greater Mexico City due to its location in a sedimentary basin, despite being ~400 km away from the epicenter (Flores-Estrella et al., 2007). Thus, it is also of great importance to map out the seismic structure of a sedimentary basin for the purpose of evaluating seismic hazards.

A third benefit of having an accurate sediment model is that it allows us to remove the strong sedimentary reverberations from seismic recordings, which can then be used for delineating the deep structure beneath the sediment cover. For example, the receiver function technique (Ammon, 1991; Burdick & Langston, 1977) generally does not work well for stations located above soft sediments as deep *P*-to-*S* conversions recorded on the surface are generally weaker and are consequently masked by sediment reverberations (Owens & Crosson, 1988; Sheehan et al., 1995). Tao et al. (2014) demonstrated that it is possible to isolate the deep signals from the sediment reverberations by using a wavefield-downward-continuation method. After the sediment response is removed, the so-called subsurface receiver functions show clear Moho *P*-to-*S* conversion and crustal multiples (between surface and Moho) and therefore are suitable for receiver function analyses.

Over the last few decades, 2-D/3-D active seismic surveys have been widely conducted to obtain high-resolution images of sedimentary structures for petroleum exploration. However, the spatial coverage of 2-D/3-D seismic surveys inside a basin is generally very limited due to the high cost of data acquisition. On the other hand, recent development in large-scale and dense passive source array seems to provide a means of achieving 3-D basin-wide sedimentary models with moderate spatial resolution. Both surface wave and body wave (BW) data have been used in resolving sedimentary structures beneath seismic stations. For example, the amplitude ratio of Rayleigh wave recorded by the vertical and radial components, known as the *Z*/*H* ratio, is very sensitive to sedimentary structures (e.g., Boore & Toksöz, 1969) and has been used to invert for sedimentary structure (e.g., Lin et al., 2012, Li et al., 2016). Sediment reverberations recorded after

teleseismic *P* waves are another type of data that are sensitive to the velocity jump at the sediment base and have been used to invert for sediment thickness and velocity (Akuhara et al., 2019; Bao & Niu, 2017). A recent study (Phạm & Tkalčić, 2017) suggests that autocorrelation of the teleseismic *P* wave coda is a promising technique for mapping shallow seismic boundaries.

In general, surface waves are sensitive to the average *S* wave velocity over a range of depths, making it difficult to constrain the accurate depth of velocity boundaries, such as the sediment base, and consequently leading to large trade-offs between depths and velocities around the boundaries. Also, it is practically difficult to estimate Z/H ratio at periods shorter than 6 s either from ambient noise or earthquake data, making it almost impossible to resolve thin sediments with thicknesses less than a few hundred meters. In contrast, teleseismic *P* waves and the following coda are of higher frequencies and are capable of resolving finer-scale structures. Using BWs alone can lead to large uncertainties in the absolute *S* wave velocity. Thus, the sediment responses of the Rayleigh wave and the teleseismic *P* wave are complementary to each other. In fact, several studies (Bodin et al., 2012; Julia et al., 2000; Kang et al., 2015; Shen, Ritzwoller, Schulte-Pelkum, & Lin, 2013) have taken advantage of this complementary nature and have jointly inverted the surface wave phase velocity and receiver function data to better constrain crustal structures. In this study, we further include the surface wave particle motion data in the joint inversion with a focus on the shallow velocity structure of sedimentary basins where it is impossible to generate receiver function data with the regular deconvolution method due to the presence of strong sediment reverberations.

2. Data and Methodology

2.1. Rayleigh Wave Z/H Ratio

Early measurements of Z/H ratio using earthquake or noise data appeared to be highly scattered, which could significantly affect the effectiveness of the joint inversion. Recent advances in high-quality instrumentation and ambient noise processing techniques lead to relatively robust measurements of Rayleigh wave Z/H (e.g., Li et al., 2016; Lin et al., 2014). In this study, we basically took the Z/H ratio data of NE68 and NE96 from Li et al. (2016).

2.2. Apparent Horizontal *P* Wave Time Delays and the Cross-Convolution Misfit Function

Receiver functions generated at seismic stations inside a sedimentary basin usually show a delayed *P* wave peak, which is caused by a delay of the *P* wave on the radial component. This horizontal *P* wave delay results from the interference of the direct *P* wave with *P*-to-*S* conversion at the sediment base and sediment reverberations. Bao and Niu (2017) found that the horizontal *P* wave delay time is a function of frequency and used this frequency-dependent delay time to constraint the *S* wave velocity and thickness of the sediment. In this study, instead of using the frequency-dependent delay times of the teleseismic *P* wave to constrain the thickness of sedimentary basins, we employ the cross-convolution misfit function (Bodin et al., 2014; Menke & Levin, 2003) as part of the objective function in the joint inversion. The cross-convolution misfit function directly involves waveform data that include the *P* wave and sedimentary reverberations and is thus expected to contain more information of the sediments than the delay times alone.

The cross-convolution misfit function is defined as the least squares difference of two convolutions between the observed and synthetic waveform data:

$$\begin{aligned} V_{\mathrm{obs}}(t)*h_{\mathrm{syn}}(t,m) &= s(t)*v(t)*I(t)*h_{\mathrm{syn}}(t,m) \\ H_{\mathrm{obs}}(t)*v_{\mathrm{syn}}(t,m) &= s(t)*h(t)*I(t)*v_{\mathrm{syn}}(t,m). \end{aligned} \tag{1}$$

Here $V_{\mathrm{obs}}(t)$ and $H_{\mathrm{obs}}(t)$ are the observed vertical and radial recordings of the *P* and its coda of a teleseismic event, while $v(t)$ and $h(t)$ are their corresponding Green's functions. $s(t)$ and $I(t)$ are the source time function of the event and the instrument response of the station, respectively. $v_{\mathrm{syn}}(t,m)$ and $h_{\mathrm{syn}}(t,m)$ are the vertical and radial components of the synthetic Green's function of a trial model m. If m is the true model, then $v_{\mathrm{syn}}(t,m)=v(t)$ and $h_{\mathrm{syn}}(t,m)=h(t)$. Therefore, the two convolutions are essentially the same. Since the convolution operation is linear and the vertical and radial Green's functions are almost independent with epicentral distances (Figure S1 in the supporting information), waveforms from different events can be stacked to improve signal-to-noise ratios (SNRs) by aligning waveforms according to their vertical

maximum amplitudes (e.g., Shearer, 1991). Before stacking, the teleseismic records are normalized by the maximum amplitude of the vertical components and are also reversed when the polarity is negative.

2.3. Joint Inversion of Surface and BW Data

Taking advantage of the complementary sensitivities of Rayleigh wave dispersion curves, Z/H ratios, and teleseismic BW data, we jointly invert all the three data sets to better constrain the basin structures. Here we employ the Delay Rejection Adaptive Metropolis Markov Chain Monte Carlo (DRAM-MCMC; Haario et al., 2006) method to perform the joint inversion. The nonlinear method is well documented in Afonso et al. (2013), and the likelihood function is defined as

$$p(d_{\mathrm{obs}}|m) = \frac{1}{\prod_{i=1}^{3}\left(\sqrt{2\pi}\sigma_i\right)} e^{-\frac{1}{2}M_{\mathrm{joint}}(m)}, \tag{2}$$

where

$$\begin{aligned} M_{\mathrm{joint}}(m) &= M_{\mathrm{PH}} + M_{\mathrm{ZH}} + M_{\mathrm{BW}} \\ &= \frac{1}{\sigma_1^2 N}\sum_{i=1}^{N}\left(\mathrm{PH}_i(m) - \mathrm{PH}_i^{\mathrm{obs}}\right)^2 + \frac{1}{\sigma_2^2 M}\sum_{j=1}^{M}\left(\mathrm{ZH}_j(m) - \mathrm{ZH}_j^{\mathrm{obs}}\right)^2 + \frac{\phi(m)}{\sigma_3^2}. \end{aligned} \tag{3}$$

Here $\mathrm{PH}_i(m)$ and $\mathrm{ZH}_i(m)$ are the calculated phase velocity and Z/H ratio of a given model m at a certain period, while $\mathrm{PH}_i^{\mathrm{osb}}$ and $\mathrm{ZH}_i^{\mathrm{obs}}$ represent the observed phase velocity and Z/H ratio at the same period. N and M are the numbers of the period at which phase velocities and Z/H ratios are measured. $\phi(m)$ is the misfit function computed from the two cross-convolutions shown in equation (1):

$$\phi(m) = 1 - \frac{\int_{T_1}^{T_2}\left\{V_{\mathrm{obs}}(t)*h_{\mathrm{syn}}(t,m)\right\}\cdot\left\{H_{\mathrm{obs}}(t)*v_{\mathrm{syn}}(t,m)\right\}dt}{\sqrt{\int_{T_1}^{T_2}\left|V_{\mathrm{obs}}(t)*h_{\mathrm{syn}}(t,m)\right|^2 dt}\cdot\sqrt{\int_{T_1}^{T_2}\left|H_{\mathrm{obs}}(t)*v_{\mathrm{syn}}(t,m)\right|^2 dt}}. \tag{4}$$

Here T_1 and T_2 define the time window that includes the direct P wave and the sediment reverberations, which are set to 5s before and 10s after the time sample with the maximum vertical amplitude. Note that the misfit function defined in equation (4) is actually similar to the normalized square difference between the two cross convolutions.

σ_1, σ_2, and σ_3 in equation (3) are the uncertainties of the three data sets, which are generally difficult to evaluate objectively. In this study, we employ a strategy proposed by Bodin et al. (2012) that treats the uncertainties as unknown model parameters, which are inverted during the inversion. We employ computer programs in seismology (Herrmann & Ammon, 2004) to calculate the synthetic phase velocity and Z/H ratio at a given period, and the Thomson-Haskell propagator matrix method (Haskell, 1962; Thomson, 1950) to compute the synthetic P wave Green's functions. We employ a simple linear model to represent the sedimentary velocity structure, which is defined by four parameters: sediment thickness, Vs at the top and the bottom of the sediment layer, and an averaged Vp/Vs of the sediment (Table S1 in the supporting information). Since the passive seismic data used in the inversion are of relatively low frequency (surface wave data $\leq$0.125 Hz and BW $\leq$0.5 Hz) and have limited resolution on details of sediment structure, a linear velocity model appears to be a suitable first-order approximation to likely more complicated velocity structure of the real sedimentary layers. A more detailed model parameterization method is elaborated in the supporting information (Brocher, 2005; Gardner et al., 1974; Haskell, 1962; Herrmann & Ammon, 2004; Shen, Ritzwoller, Schulte-Pelkum, & Lin, 2013; Thomson, 1950).

The first stage of the inversion is the burn-in period. At this stage, the code randomly generates 160,000 trial models to estimate the first-stage posterior probability. After that, the random walk is stationary and starts to produce importance sampling of the model space according to the posterior probability estimated from the burn-in period. In the second stage, we generate 80,000 candidate models, which are not fully independent. We further employ the autocorrelation method proposed by Mosegaard and Tarantola (1995) to select 1,000 independent models, which are finally used to calculate the maximum probability model. In theory, the maximum probability model is equivalent to the average model of the final ensemble of solutions.

3. Applications of the Method

3.1. Application to Synthetic Data

To illustrate the feasibility of the proposed joint inversion, we conduct tests with synthetic data generated from two velocity models. The first model has a 4-km-thick sediment layer sitting on the crystalline crust (hereafter referred to as thickSM). Details of the model are listed in Table S2, and the top 10 km of the model is plotted in Figure 1a. Based on the input model, phase velocity curves at 8–40 s, Z/H ratio curves at 8- to 40-s periods, and vertical and radial impulse responses of BWs are synthesized. The synthesized body waveforms are from 14 hypothetical events with epicentral distances from 30 to 90°. We add Gaussian noise to the synthetic phase velocity and Z/H ratio data, which has a standard deviation of 15 m/s and 3.0%, respectively. The former is based on Shen, Ritzwoller, and Schulte-Pelkum (2013), and the latter is estimated from the NECESSArray data as shown in the real data section. We also include Gaussian noise in computing the Thomson-Haskell synthetics with a SNR of 10. Here the SNR is defined as the ratio between the maximum amplitude of the signal window and the root-mean-square of the noise window. We stack the waveforms using the method described in section 2.2 and use the stacked vertical and radial waveforms to invert for the input velocity model.

We jointly invert the surface (PH+Z/H) and BW data for the shallow structure. The inverted results are plotted in the red dashed line in Figure 1a, which is almost identical to the input models (solid grey line in Figure 1a). The dispersion curves of the 1,000 resampled models in the Markov Chain (grey lines in Figures 1b and 1c) fit the observed data (solid blue squares) very well. The probability density functions of the vertical and radial impulse responses calculated from the 1,000 models are shown in Figures 1d and 1e, respectively, with the highest probability being shown in red. The predictions of these models (warm colors) match well with the observed waveforms (dashed white lines in Figures 1d and 1e), including the direct P waves and the following sediment reverberations. Figures 1f-1h show the marginal distributions of the inverted sediment thickness, the surface S wave velocity, and the Vp/Vs ratio of the sediment layer, respectively. All of the three parameters follow an approximately Gaussian distribution with small standard deviations, suggesting that they are tightly constrained by the joint inversion. For comparison, we also conduct two more inversions: one using only the Rayleigh wave data (PH+Z/H) and the other using BW data alone. The two inverted models are also plotted in blue dotted and green dash-dotted lines in Figure 1a, respectively, together with the input model (grey solid line) as well as the joint inversion model (red dashed line). We notice that the BW-based model exhibits an unusual trade-off between the sediment depth and velocity, which is attributed to the higher recovered Vp/Vs ratio (2.87) as compared to the input Vp/Vs ratio (2.0). A quantitative comparison between the input model and three inverted models is further shown in Table S2. It is apparent that the joint inversion best recovers the input model in all aspects.

The second model has a thin and unconsolidated sediment layer with a thickness of 0.5 km, which we refer to as thinSM. Details of the model parameter are listed in Table S3. We follow the above approach and conduct one joint and two separate inversions. The results are shown in Figure S2 and listed in Table S3, which again indicates that the joint inversion does a much better job than the two independent inversions in terms of recovering the input model.

3.2. Application to Field Data

We also apply the joint inversion method to waveform data recorded at two broadband stations (NE68 and NE96) inside the Songliao Basin in northeast China (Figure S3). The two stations belong to the NECESSArray (NorthEast China Extended SeiSmic Array; Steve & Jim, 2009) project, a temporal deployment of 127 broadband seismic stations in northeast China between September 2009 and September 2011. Station NE68 is located in the southern Songliao Basin with relatively thin sedimentary accumulation (Wei et al., 2010); while station NE96 is located in the northern Songliao Basin near the city Daqing (Figure S3), which is named after China's largest oil field, Daqing (also known as Taching) Oil Field inside the central downwarp of the basin (Feng et al., 2010).

We obtain the phase velocities and Z/H ratios in the periods of 8-40 s of the two stations from Guo et al. (2015) and Li et al. (2016), respectively. We select teleseismic records at the two stations from earthquakes with a magnitude greater than 6.0 and an epicentral distance between 30 and 90°. We first align the waveform records at the maximum amplitude of the P waves on the vertical components, which is set to zero

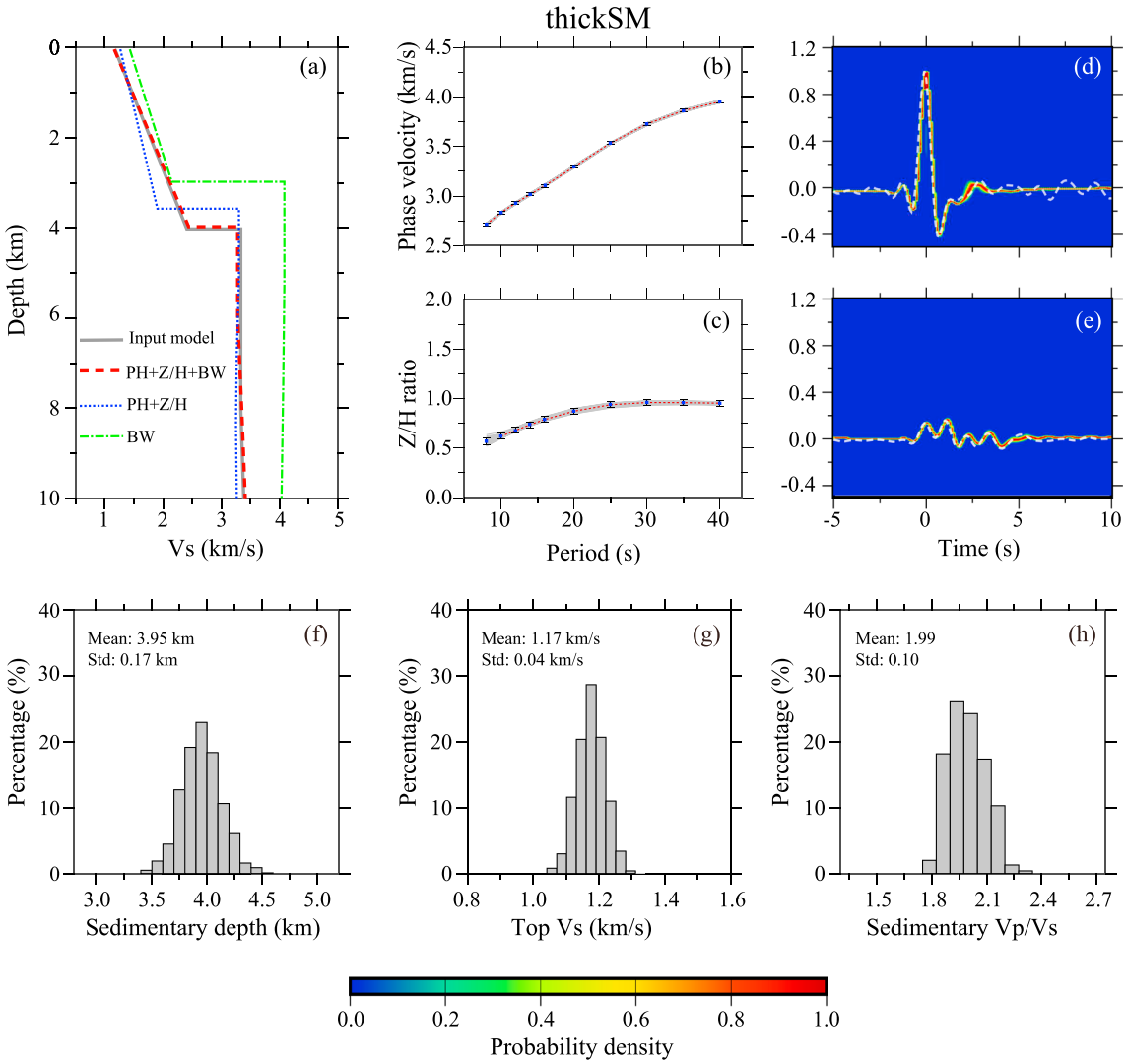

Figure 1. Synthetic tests with the thickSM model. (a) The input model (grey solid line) is shown together with three resulting models from one joint (red dashed line) and two separate inversions (blue dashed line and green dash-dotted line). PH, Z/*H*, and BW represent Rayleigh wave phase velocity, Rayleigh wave *Z*/*H* ratio, and teleseismic body wave data, respectively. (b) The synthetic phase velocity data with an uncertainty of 15 m/s (blue squares with error bars connected by the red dotted line) computed from the input model are shown together with calculated phase velocities of the 1,000 resampled models (grey solid lines). (c) Same as (b) except for *Z*/*H* ratio data. The assigned uncertainty here is 3%. (d) The white dashed lines show the stacked vertical component of the 14 hypothetic events, and the background shows the probability density function of the vertical component synthetic seismograms of the 1,000 resampled models. (e) Same as (d) but for the horizontal component. (f–h) The marginal distributions of sediment thickness, surface Vs, and average Vp/Vs ratio of the sediment layer.

time. As mentioned before, if the maximum amplitude is negative, we reverse the polarity of the recordings by multiplying them with minus one. We then stack all the vertical and radial records separately to generate hypothetic teleseismic records of the vertical and radial components. The stacked waveforms are further band-pass filtered between 0.05 and 0.5 Hz, which are shown in Figures 2c and 2i, respectively.

We conduct a joint inversion of the three types of data to obtain a 1-D Vs profile beneath each station. The inverted results of NE68 and NE96 are shown in Figures 2a-2f and 2g-2l. In general, the calculated phase velocities and *Z*/*H* ratios of the 1,000 independent models (thin grey in Figures 2a and 2b and 2g and 2h) fit the observed data (black crosses) well. The probability density functions of the two cross convolutions, $V_{obs}(t)$*$h_{syn}(t,m)$ and $H_{obs}(t)$*$v_{syn}(t,m)$, shown in Figures 2e and 2f and 2k and 2l, appear to be similar to each other. In fact, the cross-correlation coefficient between the pairs is 0.95 for NE68 and 0.92 for NE96, which implies that stacked waveform data at these two stations are well matched. The sediment layer beneath NE68 is 0.45±0.07 km thick (Figure 2d) with an average sediment Vp/Vs ratio of 2.77±0.26. The *S* wave

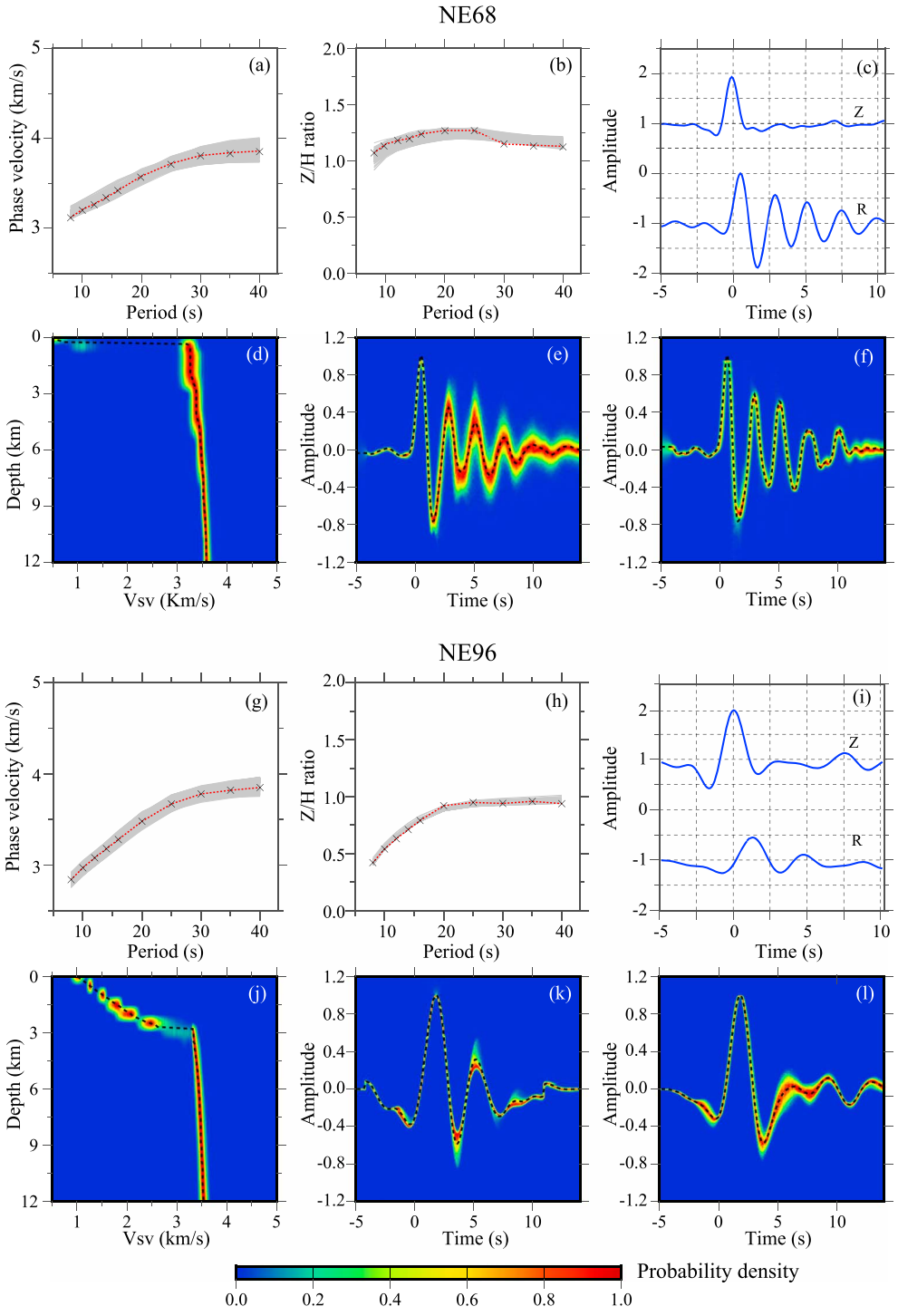

Figure 2. Field data application. (a) The measured Rayleigh wave velocities (black crosses connected by the red dotted line) at NE68 are shown together with calculated phase velocities of the 1,000 resampled models (grey solid lines). (b) Same as (a) except for Z/H ratios. Note that the model predictions seem to be lower than the observed Z/H data before 25 s but larger after 30 s, which might suggest that there is a systematic bias in the Z/H measurements from ambient noise (<25 s) and earthquake (≥25) data. (c) Stacked vertical and horizontal components of the teleseismic *P* and coda waves recorded at NE68. (d) Color map showing the posterior density function of the inverted Vs with the black dotted line representing the maximum probability model. (e and f) The color contours showing the probability density functions of the cross convolutions between the data and 1,000 independent models. The black dotted lines are the cross convolutions between the observed waveforms and the synthetic Green's functions of the maximum probability model. (g–l) The same as (a)-(f) except for NE96.

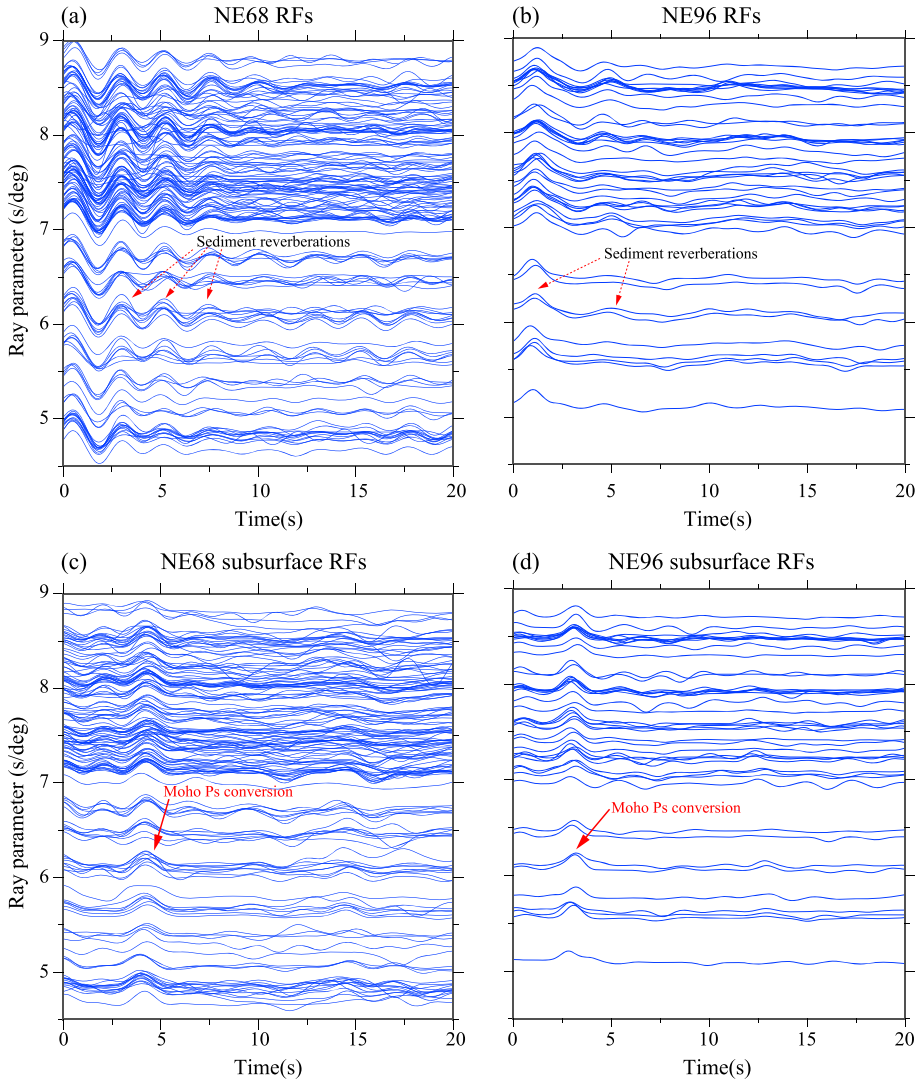

Figure 3. Surface and subsurface receiver functions. (a) Surface and (c) subsurface receiver functions (RFs) recorded at NE68 are plotted as a function of the ray parameter. Note the large-amplitude sediment reverberations in (a) and the isolated Moho Ps in (c). (b and d) Similar to (a) and (c), respectively, except for NE96.

velocity of the sediment layer is very low, which is 0.47±0.11 km/s at the surface and increases to 0.79±0.24 km/s at the bottom of the layer, suggesting that the sediments are largely unconsolidated at this location. The resulting sedimentary layer underneath NE96 is ~2.90±0.21 km thick with an average Vp/Vs ratio of 2.20±0.23 and an *S* wave velocity increasing from 0.99±0.07 km/s at the surface to 2.50±0.21 km/s at the bottom of the layer. The uncertainties here are calculated from the standard deviation of the 1,000 resampled models and are generally acceptable.

We could not find any well log and active source profiles near the two stations for direct comparisons of our models. Therefore, we decide to take an alternative approach to verify the 1-D velocity models by evaluating their predictability of the teleseismic *P* coda. In other words, if a model is correct, it is expected to be able to generate the strong reverberations shown in receiver function data, and we can use the model predictions to remove these reverberations and to extract the Moho Ps conversion from the data.

As shown in Figures 3a and 3b, sediment reverberations are the predominant signals of the surface receiver functions recorded at the two stations. We then use the two 1-D models shown in Figure 2 and adopt a wavefield-downward-downward-continuation technique (Tao et al., 2014) to strip off the sedimentary responses from the receiver functions. The corrected receiver functions at the two stations, which can be

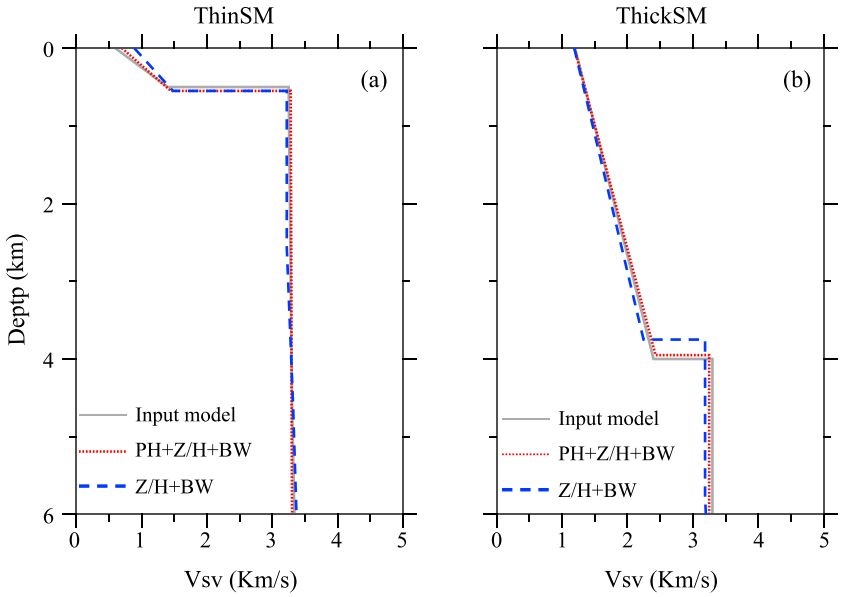

Figure 4. Single-station inversion results. (a) The input thinSM model (grey solid line) is shown together with the two resulting models from two joint inversions with (red dotted line) or without the phase velocity data (blue dashed line). (b) Same as (a) except for the thickSM model. PH, Z/H, and BW represent Rayleigh wave phase velocity, Rayleigh wave Z/H ratio, and teleseismic body wave data, respectively.

considered as being recorded at stations projected down to the base of the sediments and are referred as to subsurface receiver functions by Tao et al. (2014), are shown in Figures 3c and 3d, respectively. It is clear that the large-amplitude reverberations shown in the surface receiver functions (Figures 3a and 3b) disappear in the subsurface receiver functions (Figures 3c and 3d). Meanwhile, the subsurface receiver functions show clear signals at ~4.5s and ~3.0s in Figures 3c and 3d, respectively. The arrival time of the two signals increases slightly with increasing ray parameter, suggesting that they are the *P*-to-*S* conversions at the Moho interface.

4. Discussion

We have assumed that the vertical and horizontal Green's functions, $v_{syn}(t,m)$ and $h_{syn}(t,m)$, remain the same over the teleseismic distances of 30-90°, which are used to match the stacked waveforms of the two components, $V_{obs}(t)$ and $H_{obs}(t)$. This assumption helps our inversions in two aspects: (1) it significantly reduces the number of body waveforms to be fitted, leading to more efficient inversions, and (2) the stacked teleseismic data are of much higher SNR as compared to the individual ones, making the inversion more robust. On the other hand, since the ray parameters of the *P*-to-*S* conversion at the base of the sediments and sedimentary reverberations are marginally different from those of the direct *P* waves, therefore, the impulse responses to incident *P* waves are expected to vary slightly with the incident angle, which is clearly shown in Figure S1. The stacked waveforms have relative low cross-correlation coefficients with those recorded at large or small epicentral distances. However, the *S* wave velocity inside the sediments is generally very low; therefore, the sediment Ps and reverberations propagate nearly vertically (incident angle of ~2°) inside the sediments even if the incident angle of the teleseismic *P* changes from 14 to 28°, which corresponds to an epicentral distance of 90 and 30°, respectively. This means that changes in sediment response to epicentral distance are almost negligible, although it is not true when the crustal response is considered (Chen & Niu, 2013).

In our joint inversion, we combine Rayleigh wave phase velocity, Rayleigh wave Z/H ratio, and teleseismic waveforms to jointly invert for sedimentary structures. In the inversion, Rayleigh wave phase velocity and Z/H ratio mainly help constrain smoothly varying velocities, while BW data contribute to constraining the sediment-crystalline boundary. Both the Z/H ratio and the cross convolutions of teleseismic *P* waves can be computed with data recorded by a single seismic station, while phase velocities have to be obtained

from surface wave tomography that requires a seismic array, which might not be available in some cases. We thus examine whether or not excluding the phase velocity data in the joint inversion can still achieve similar results. To do so, we perform two additional inversions by using the Z/H ratio and cross-convolution data of the two synthetic models, thickSM and thinSM, described in section 3.1. We perform essentially the same joint inversions of section 3 except that we assign a zero weight to the phase velocity data. The resulting two models are shown in blue dashed lines in Figures 4a and 4b and further listed in Tables S2 and S3. For comparison, we also show the input model (grey solid line) and the joint inversion model (red dotted line) with three types of data. In the case of thinSM (Figure 4a), the two models inverted with or without the phases velocity data are quite similar; both are very close to the input model. In the case of thickSM (Figure 4b), the resulting sedimentary depth is 3.75 km, which is 0.25 km less than the input value of 4 km. This discrepancy is likely caused by the relatively lower sensitivity of the Z/H ratio data to deep structures as compared to phase velocity data. We find that if we extend the period band of the Z/H ratio data to 90s, we can almost recover the input model (3.95 km). The above investigation thus suggests that it is possible to constrain sedimentary structures beneath a seismic station using Rayleigh wave Z/H ratio and teleseismic cross-convolution data. Therefore, the joint inversion method proposed here can be extended to single station recordings.

5. Conclusions

In this study, we develop a method by jointly inverting Rayleigh wave phase velocity, Rayleigh wave Z/H ratio, and teleseismic BWs for sedimentary structures. Numerical tests with synthetic data of two end models indicate that the joint inversion is effective in resolving sedimentary structures with varying thicknesses. We further apply the joint inversion to seismic records of two broadband stations located within the Songliao Basin. The resulting models beneath the two stations show a large contrast in sediment structure between the southern and northern parts of the basin. The inverted models are capable of removing sedimentary reverberations from the teleseismic data recorded at the two stations. We further show that our method is applicable to areas where only sparse seismic stations are available and array-based seismic processing techniques can be implemented.

Acknowledgments
The waveform data can be downloaded from www.fdsn.org/networks/detail/YP_2009. We also thank the three anonymous reviewers for their constructive comments and suggestions, which significantly improved the quality of this paper. This work was supported by the National Key Research and Development Program of China (2017YFC1500300), the National Natural Science Foundation of China (41630209), and the Australian Research Council Future Fellowship (FT130101220). This is contribution 1357 from the ARC Centre of Excellence for Core to Crust Fluid Systems (http://www.ccfs.mq.edu.au) and 1318 in the GEMOC Key Centre (http://www.gemoc.mq.edu.au).

References

Afonso, J. C., Fullea, J., Griffin, W. L., Yang, Y., Jones, A. G., Connolly, J. A. D., & O'Reilly, S. Y. (2013). 3-D multiobservable probabilistic inversion for the compositional and thermal structure of the lithosphere and upper mantle. I: A priori petrological information and geophysical observables. *Journal of Geophysical Research: Solid Earth*, *118*, 2586–2617. https://doi.org/10.1002/jgrb.50124

Akuhara, T., Bostock, M. G., Plourde, A. P., & Shinohara, M. (2019). Beyond receiver functions: Green's function estimation by transdimensional inversion and its application to OBS data. *Journal of Geophysical Research: Solid Earth*, *124*, 1944–1961. https://doi.org/10.1029/2018JB016499

Ammon, C. J. (1991). The isolation of receiver effects from teleseismic *P* waveforms. *Bulletin of the Seismological Society of America*, *81*, 2504–2510.

Bao, Y., & Niu, F. (2017). Constraining sedimentary structure using frequency-dependent *P* wave particle motion: A case study of the Songliao Basin in NE China: Sediment constrained by *P* wave splitting. *Journal of Geophysical Research: Solid Earth*, *122*, 9083–9094. https://doi.org/10.1002/2017JB014721

Bodin, T., Smbridge, M., Rawlinson, N., & Arroucau, P. (2012). Transdimensional tomography with unknown data noise. *Geophysical Journal International*, *189*(3), 1536–1556.

Bodin, T., Yuan, H., & Romanowicz, B. (2014). Inversion of receiver functions without deconvolution—Application to the Indian craton. *Geophysical Journal International*, *196*, 1025–1033. https://doi.org/10.1093/gji/ggt431

Bonilla, L. F., Steidl, J. H., Lindley, G. T., Tumarkin, A. G., & Archuleta, R. J. (1997). Site amplification in the San Fernando Valley, California: Variability of site-effect estimation using the *S*-wave, coda, and H/V methods. *Bulletin of the Seismological Society of America*, *87*, 710–730.

Boore, D. M., & Toksöz, M. N. (1969). Rayleigh wave particle motion and crustal structure. *Bulletin of the Seismological Society of America*, *59*(1), 331–346.

Brocher, T. M. (2005). Empirical relations between elastic wavespeeds and density in the Earth's crust. *Bulletin of the Seismological Society of America*, *95*(6), 2081–2092. https://doi.org/10.1785/0120050077

Burdick, L., & Langston, C. (1977). Modeling crustal structure through the use of converted phase in teleseismic body-wave forms. *Bulletin of the Seismological Society of America*, *67*(3), 677–691.

Chen, Y., & Niu, F. (2013). Ray parameter based stacking and enhanced preconditioning for stable inversion of receiver function data. *Geophysical Journal International*, *194*(3), 1682–1700. https://doi.org/10.1093/gji/ggt179

Feng, Z., Jia, C., Xie, X., Zhang, S., Feng, Z., & Cross, T. A. (2010). Tectonostratigraphic units and stratigraphic sequences of the nonmarine Songliao Basin, northeast China. *Basin Research*, *22*(1), 79–95. https://doi.org/10.1111/j.1365-2117.2009.00445.x

Flores-Estrella, H., Yussim, S., & Lomnitz, C. (2007). Seismic response of the Mexico City Basin: A review of twenty. *Natural Hazards*, *40*(2), 357–372. https://doi.org/10.1007/s11069-006-0034-6

Gardner, G. H. F., Gardner, L. W., & Gregory, A. R. (1974). Formation velocity and density—The diagnostic basis for stratigraphic traps. *Geophysics*, *39*(6), 770–780. https://doi.org/10.1190/1.1440465

Guo, Z., Chen, Y., Ning, J., Feng, Y., Grand, S. P., Niu, F., et al. (2015). High resolution 3-D crustal structure beneath NE China from joint inversion of ambient noise and receiver functions using NECESSArray data. *Earth and Planetary Science Letters*, *416*, 1–11. https://doi.org/10.1016/j.epsl.2015.01.044

Haario, H., Laine, M., Mira, A., & Saksman, E. (2006). DRAM: Efficient adaptive MCMC. *Statistics and Computing*, *16*(4), 339–354. https://doi.org/10.1007/s11222-006-9438-0

Haskell, N. A. (1962). Crustal reflection of plane *P* and SV waves. *Journal of Geophysical Research*, *67*(12), 4751–4768. https://doi.org/10.1029/JZ067i012p04751

Herrmann, R. B., & Ammon, C. J. (2004). Surface waves, receiver functions and crustal structure, in Computer Programs in Seismology, Version 3.30. http://www.eas.slu.edu/eqc/eqc_cps/CPS/CPS330/cps330c.pdf, last accessed 14 July 2011.

Hough, S. E., Friberg, P. A., Busby, R., Field, E. F., Jacob, K. H., & Borcherdt, R. D. (1990). Sediment-induced amplification and the collapse of the Nimitz Freeway. *Nature*, *344*(6269), 853–855. https://doi.org/10.1038/344853a0

Julia, J., Ammon, C. J., Herrmann, R. B., & Correig, A. M. (2000). Joint inversion of receiver function and surface wave dispersion observations. *Geophysical Journal International*, *143*(1), 99–112. https://doi.org/10.1046/j.1365-246x.2000.00217.x

Kang, D., Shen, W., Ning, J., & Ritzwoller, M. H. (2015). Seismic evidence for lithospheric modification associated with intracontinental volcanism in Northeastern China. *Geophysical Journal International*, *204*, 215–235.

Li, G., Chen, H., Niu, F., Guo, Z., Yang, Y., & Xie, J. (2016). Measurement of Rayleigh wave ellipticity and its application to the joint inversion of high-resolution *S* wave velocity structure beneath northeast China. *Journal of Geophysical Research: Solid Earth*, *121*, 864–880. https://doi.org/10.1002/2015JB012459

Lin, F.-C., Schmandt, B., & Tsai, V. C. (2012). Joint inversion of Rayleigh wave phase velocity and ellipticity using USArray: Constraining velocity and density structure in the upper crust. *Geophysical Research Letters*, *39*, L12303. https://doi.org/10.1029/2012GL052196

Lin, F. C., Tsai, V. C., & Schmandt, B. (2014). 3-D crustal structure of the western United States: application of Rayleigh-wave ellipticity extracted from noise cross-correlations. *Geophysical Journal International*, *198*(2), 656–670. https://doi.org/10.1093/gji/ggu160

Menke, W., & Levin, V. (2003). The cross-convolution method for interpreting SKS splitting observations, with application to one and two-layer anisotropic earth models. *Chinese Journal of Geophysics*, *154*(2), 379–392. https://doi.org/10.1046/j.1365-246X.2003.01937.x

Mosegaard, K., & Tarantola, A. (1995). Monte Carlo sampling of solutions to inverse problems. *Journal of Geophysical Research*, *100*(B7), 12,431–12,447. https://doi.org/10.1029/94JB03097

Owens, T. J., & Crosson, R. S. (1988). Shallow structure effects on broadband teleseismic *P* waveforms. *Bulletin of the Seismological Society of America*, *78*, 96–108.

Phạm, T. S., & Tkalčić, H. (2017). On the feasibility and use of teleseismic *P* wave coda autocorrelation for mapping shallow seismic discontinuities. *Journal of Geophysical Research: Solid Earth*, *122*, 3776–3791. https://doi.org/10.1002/2017JB013975

Shearer, P. (1991). Imaging global body wave phases by stacking long-period, seismograms. *Journal of Geophysical Research*, *96*(B12), 20,353–20,364. https://doi.org/10.1029/91JB00421

Sheehan, A. F., Abers, G. A., Jones, C. H., & Lerner-Lam, A. L. (1995). Crustal thickness variations across the Colorado Rocky Mountains from teleseismic receiver functions. *Journal of Geophysical Research*, *100*(B10), 20,391–20,404. https://doi.org/10.1029/95JB01966

Shen, W., Ritzwoller, M. H., Schulte-Pelkum, V., & Lin, F.-C. (2013). Joint inversion of surface wave dispersion and receiver functions: A Bayesian Monte-Carlo approach. *Geophysical Journal International*, *192*(2), 807–836. https://doi.org/10.1093/gji/ggs050

Shen, W., Ritzwoller, M. H., & Schulte-Pelkum, V. A. (2013). 3-D model of the crust and uppermost mantle beneath the Central and Western US by joint inversion of receiver functions and surface wave dispersion. *Journal of Geophysical Research: Solid Earth*, *118*, 262–276. https://doi.org/10.1029/2012JB009602

Steve G., & Jim N. (2009). Collaborative research: Northeast China extended seismic array: Deep subduction, mantle dynamics and lithospheric evolution beneath Northeast China. International Federation of Digital Seismograph Networks. Dataset/Seismic Network. https://doi.org/10.7914/SN/YP_2009

Tao, K., Niu, F., Ning, J., Chen, Y. J., Grand, S., Kawakatsu, H., et al. (2014). Crustal structure beneath NE China imaged by NECESSArray receiver function data. *Earth and Planetary Science Letters*, *398*, 48–57. https://doi.org/10.1016/j.epsl.2014.04.043

Thomson, W. T. (1950). Transmission of elastic waves through a stratified solid medium. *Journal of Applied Physics*, *21*(2), 89–93. https://doi.org/10.1063/1.1699629

Wei, H. H., Liu, J.-L., & Meng, Q. (2010). Structural and sedimentary evolution of the southern Songliao Basin, northeast China, and implications for hydrocarbon prospectivity. *AAPG Bulletin*, *94*(4), 533–566. https://doi.org/10.1306/09080909060